



Preparation of porous carbons by hydrothermal carbonization and KOH activation of lignite and their performance for electric double layer capacitor

Yan Wu, Jing-Pei Cao*, Xiao-Yan Zhao, Zhi-Qiang Hao, Qi-Qi Zhuang, Jun-Sheng Zhu, Xing-Yong Wang, Xian-Yong Wei

Key Laboratory of Coal Processing and Efficient Utilization (Ministry of Education), China University of Mining & Technology, Xuzhou, 221116, Jiangsu, China



ARTICLE INFO

Article history:

Received 20 June 2017

Received in revised form 15 August 2017

Accepted 29 August 2017

Available online 1 September 2017

Keywords:

Lignite

Hydrothermal carbonization

Porous carbons

Electric double layer capacitor

ABSTRACT

A series of porous carbons (PCs) were obtained from Shengli lignite (SL) via hydrothermal carbonization (HTC) pre-treatment and followed by chemical activation with KOH. The effects of preparation parameters including HTC temperature, KOH-hydrochar ratio and activation temperature on pore structure and the electrochemical performances of PCs were investigated in details. The PCs are mainly micropores structure according to the N_2 adsorption-desorption isotherms test and the highest specific surface area (SSA) is up to $3162\text{ m}^2\text{ g}^{-1}$. The SSA and total pore volume of PCs with HTC pre-treatment are larger than that without HTC treatment. The electrochemical performances of the symmetric electric double layer capacitor (EDLC) fabricated from these PC electrodes were tested by galvanostatic charge-discharge, cyclic voltammetry and electrochemical impedance spectroscopy. All the PCs as electrode for EDLC exhibit ideal capacitive behaviors in 6 M KOH electrolyte. The specific capacitance of 200-HTC-800-3 can reach as high as 295 F g^{-1} at the current density of 40 mA g^{-1} and still retained 210 F g^{-1} at the current density of 10 A g^{-1} . It also shows excellent electrochemical cycle performance that after 15000 cycles the specific capacitance value almost not decay. The processes used to produce the PCs can reduce the energy consumption compared to the traditional carbonization-activation method.

© 2017 Elsevier Ltd. All rights reserved.

1. Introduction

As a highlight energy storage device, supercapacitors have attracted much attention due to their high power densities, fast charge-discharge rates, long cycling life and excellent stability [1–4]. Supercapacitors have a wide range of applications, such as hybrid electrical vehicles, communication devices, portable devices and electronic devices [5,6]. According to the storage mechanism, the supercapacitors can be classified into two categories, electric double layer capacitor (EDLC) and pseudocapacitor [7]. EDLC shows that the double layer is formed at the electrode/electrolyte interface to storage energy, while pseudocapacitor exhibits the reversible redox reaction in the electrodes [8,9].

The electrochemical performances of EDLC are affected by the surface property and specific surface area (SSA). Porous materials with high SSA and appropriate porosity distribution are beneficial

to the improvement of electrochemical performances. Porous materials with excellent electrical conductivity and porous structure are widely used for EDLC, such as porous carbons (PCs) [10–12], carbon nanotubes (CNTs) [13,14], graphene sheets [15,16], carbon aerogels [17] and carbon nanofibers [18]. Among that, PCs are always one of the most investigated electrode materials because of the large SSA, moderate cost and good electrical properties. The PC electrode materials were mainly prepared from biomass wastes, coal, pitch, petroleum and their derived products through chemical activation or physical activation. While in a variety of raw materials, coal is still main material for PCs due to its easy availability, low cost and high carbon contain.

Hydrothermal carbonization (HTC) is an alternative thermochemical synthesis method to produce functional carbon materials with high concentrations of oxygenated functional groups [19–21]. The hydrochar rich in oxygenated functional groups makes it suitable for a lot of applications, such as adsorption [22], drug delivery [23], catalyst supporter [24,25] and PCs synthesis [26,27]. Furthermore, the presence of oxygen groups in the precursor improves the activity of activating agent and thus causes the

* Corresponding author.

E-mail addresses: caojingpei@cumt.edu.cn, beyondcao@hotmail.com (J.-P. Cao).

increase in the porosity of the activated carbon [27,28]. Hydrothermal treatment is environmentally friendly as the reactions are carried out in the enclosed system conditions.

Recently, several researchers synthesized the PCs and carbon spheres through hydrothermal treatment with biomass [29–31]. It is well-known that low-rank coal, such as lignite, have high moisture, low calorific value and high volatiles, which are not suitable for coking raw materials. Lignite are frequently carbonized and upgraded by HTC treatment [32,33]. However, the PCs derived from the lignite with HTC treatment and applied in EDLC are rarely reported.

In this study, lignite were used as the raw material to prepare PCs by two-step method. Firstly, lignite were HTC pre-treated in Teflon-lined autoclave and then the hydrochar was activated with KOH. The PCs were characterized by the pore size analyzer, X-ray diffractometer (XRD), scanning electron microscopy (SEM) and Fourier transform infrared spectrometer (FTIR). The PCs were used as electrode material to investigate the electrochemical properties of EDLC in 6 M KOH aqueous electrolyte by galvanostatic charge-discharge (GCD), cyclic voltammetry (CV) and electrochemical impedance spectroscopy (EIS).

2. Experimental

2.1. Materials

Shengli lignite (SL) from Xilin Gole of Inner Mongolia, China were used as the raw material in this study. The proximate and ultimate analyses of SL were listed in Table 1. Analytical grade KOH was provided by Xilong Chemical Co. Ltd.

2.2. Preparation of PCs

The PCs were prepared through two-stage process involving HTC and chemical activation with KOH. 5.0 g of SL and 40 mL deionized water were added to a 100 mL Teflon-lined autoclave and heated at a prescribed temperatures of 160, 180, 200 and 220 °C for 8 h. After the autoclave was cooled down to room temperature, the resulted product was filtered and washed by deionized water several times followed by desiccation at 100 °C for 24 h. The obtained hydrothermal produce was denoted as T-hydrochar, where T represents for the HTC temperature. The hydrochar was then mixed with KOH and activated in a horizontal tube furnace with a heating rate of 10 °C min⁻¹ up to the final temperature (600, 700, 800 and 900 °C) and held for 90 min under Ar atmosphere. After cooling down, the activated sample was washed with 2 M HCl and subsequently washed several times with hot deionized water and finally with cooling deionized water until neutral. Then the sample was dried at 150 °C in vacuum for 3 h. The obtained PC was named as T-HTC-X-Y, where T represents the HTC temperature, X represents the final heating temperature and Y represents the mass ratio of KOH and hydrochar. AC-800-3 was that the SL was directly activated with KOH at the temperature 800 °C and the KOH/SL ratio of 3. The yield of PCs was estimated by Eq. (1).

$$Y = \frac{M_1}{M_2} \times 100\% \quad (1)$$

Where M_1 is the weight of PCs, M_2 is the weight of SL.

2.3. Characterization

SEM images were obtained using a Merlin Zeiss to observe the morphology of the samples. X-ray diffraction (XRD) measurements were performed on a Bruker D8 Advance diffractometer with Cu K α radiation. The surface functional groups were analyzed by a

Table 1
Proximate and ultimate analyses of SL.

Proximate analysis (wt%)				Ultimate analysis (wt%, daf)				S _{t,d}	H/C
M _{ar}	A _d	VM _d	FC _d ^b	C	H	N	O ^b		
12.8	18.7	43.6	37.7	67.5	4.9	1.3	25.8	0.5	0.9

A: ash; M: moisture; FC: fixed carbon; VM: volatile matter; ar: as received basis; d: dried basis; S_{t,d}: total sulfur in dried basis; ^b Calculated by difference.

Nicolet Magna 560 FTIR spectrometer. Raman analysis were carried out on a Bruker Senterra Raman Spectroscopy with 532 nm laser excitation. N₂ adsorption-desorption isotherms were measured at -196 °C with a Gold APP V-Sorb 4800TP instrument. The SSA was obtained by applying the Brunauer-Emmett-Teller (BET) method. Micropore surface area and micropore volume were calculated by using the t-plot method. Total pore volume was determined at a relative pressure P/P₀ of 0.99. The pore size distribution was calculated from N₂ sorption data using Density Functional Theory (DFT) model method. Thermogravimetric (TG) analysis of SL and 200-hydrochar were measured by a Mettler-Toledo TGA/DSC1 analyzer. Transmission electron microscope (TEM) images were carried out with an FEI Tecnai G2 F20 microscope. X-ray photoelectron spectroscopy (XPS) data were collected in Thermo ESCALAB 250Xi apparatus.

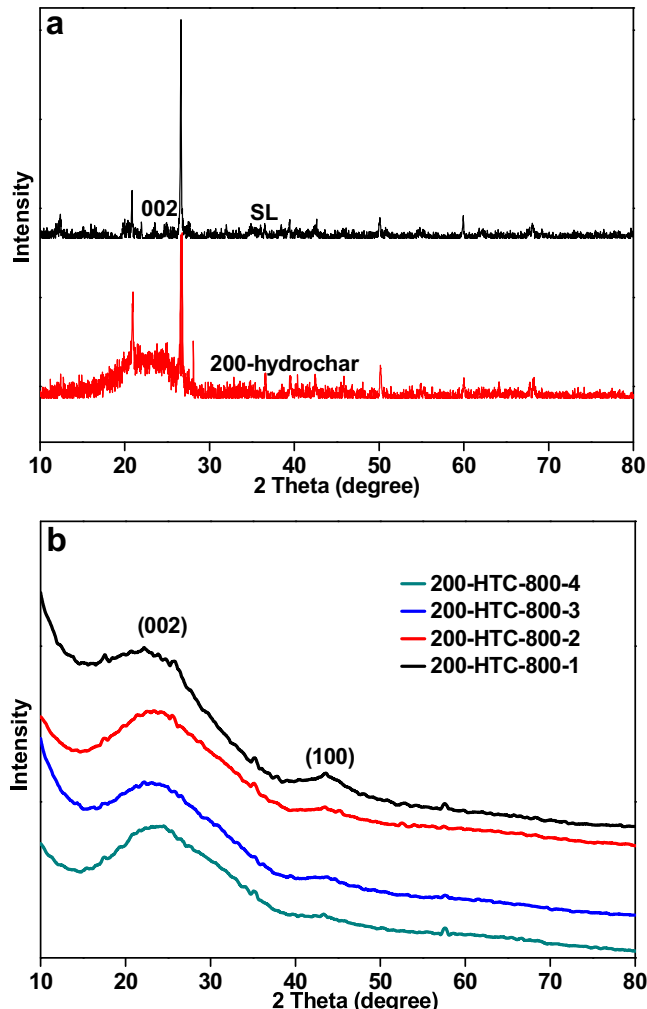


Fig. 1. XRD patterns of SL and 200-hydrochar (a) and PCs from different KOH-hydrochar ratios (b).

2.4. Electrochemical measurements

The working electrodes were prepared by the mixture of 85 wt% PC, 10 wt% acetylene black and 5 wt% polytetrafluoroethylene (PTFE). The mixture was firstly grinded in an agate mortar until a uniform and slice sheet was obtained. Then the sheet was pressed to 13 mm disc and a nickel foam was used as current collector. Two electrodes (*ca.* 10.0 mg of activated materials was loaded in each electrode) were assembled in a CR2032 coin cell with a polymer separator between the electrodes. Meanwhile, the electrolyte solution is 6 M KOH. CV and EIS tests were conducted on an Ivium Vertex electrochemical workstation. GCD test was carried out in NEWARE battery test system. The C_s of the electrode was calculated by Eq. (2) according to the discharge curve. Energy density (Wh kg^{-1}) and power density (W kg^{-1}) were obtained by Eqs. (3) and (4).

$$C_s = 2 \frac{I\Delta t}{m\Delta V} \quad (2)$$

$$E = \frac{C_s \Delta V}{8} \times \frac{1000}{3600} \quad (3)$$

$$P = \frac{E}{\Delta t} \times 3600 \quad (4)$$

Where C_s (F g^{-1}) is the specific capacitance of EDLC, Δt (s) represents the discharge time, ΔV (mV) is the discharge voltage and m (mg) is the mass of a single electrode.

The impedance is consisted of the real impedance $Z'(\omega)$ and imaginary impedance $Z''(\omega)$

$$Z(\omega) = Z'(\omega) + jZ''(\omega) \quad (5)$$

Detailed information can be found in reference [34]. The capacitance $C(\omega)$ can be defined as

$$C(\omega) = C' - jC''(\omega) \quad (6)$$

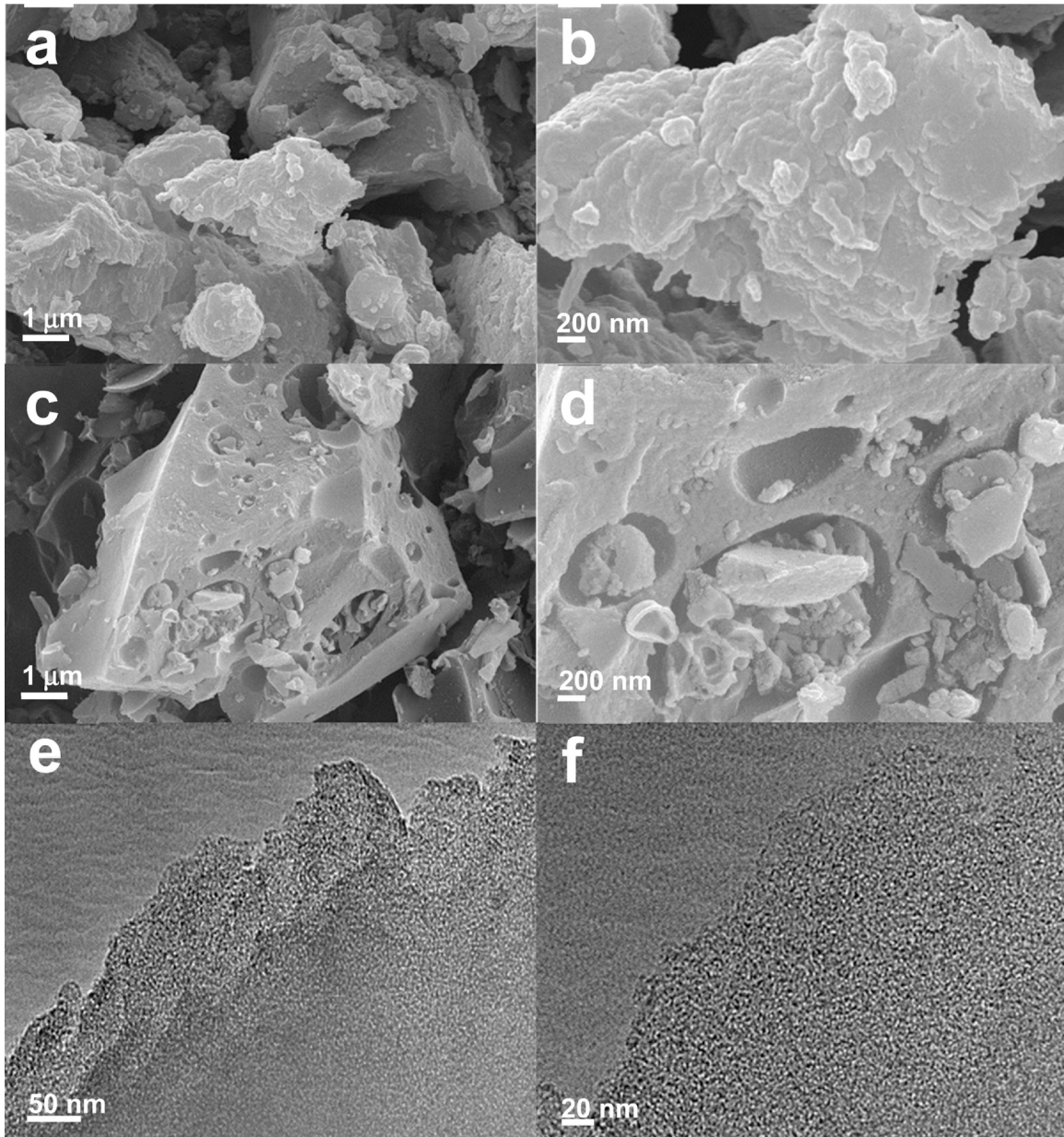


Fig. 2. SEM images of 200-hydrochar (a and b), 200-HTC-800-3 (c and d) and TEM images of 200-HTC-800-3 (e and f).

Where $C'(\omega)$ is the real part of capacitance and $C''(\omega)$ is the imaginary part of capacitance. Then, the imaginary part of capacitance can be calculated based on impedance data via Eq. (7).

$$C'' = \frac{Z'(\omega)}{\omega Z''(\omega)}^2 \quad (7)$$

3. Results and discussion

3.1. Structural characterization

The crystallographic structure of samples can be characterized by XRD. Fig. 1a shows the XRD patterns of SL and 200-hydrochar. There is an obvious diffraction peak (002) at about 20° (21° – 26°) which is correspond to the structure of amorphous layers [35]. The intensity of diffraction peak at 26° has a little decrease and the diffraction peak (002) become a weak broad, illustrating the decrease of graphitization degree and an amorphous carbon phase after HTC [36,37]. The XRD patterns of PCs with different KOH-hydrochar ratios (Fig. 1b) show two broad diffraction peaks at 24° (002) and 44° (100), ascribing to the (002) and (100) diffraction patterns of the amorphous carbon. As shown in Fig. 1b, the peak at 44° (100) became weak and almost disappeared with raising the ratio of KOH-hydrochar, suggesting the high content of KOH could be destroyed the graphitic crystalline structures [38]. SEM images of the surface micromorphology of samples are shown in Fig. 2. It can be seen that, many large particles dispersed unevenly in 200-hydrochar. The surface has a great change after the activation by KOH as shown in Figs. 2c and 2d. The sample surface of 200-HTC-800-3 is rough with a lot of small pores and the SSA increase after KOH activation. For further observation the morphology and structure of 200-HTC-800-3, TEM images were obtained. As shown in Figs. 2e and 2f, the amorphous porous structure of the carbon has some partially aligned graphitic layers. In addition, the thermal stability of the sample is enhanced after HTC pre-treated (Fig. S2).

Fig. 3a shows the FTIR spectra of SL, 200-hydrochar and 200-HTC-800-3 over the range of 4000 – 400 cm^{-1} . The band at 3432 cm^{-1} is belong to $-\text{OH}$ stretching. The strong bands at 1620 cm^{-1} and 1395 cm^{-1} are attributed to $\text{C}=\text{C}$ stretching [39] and $\text{C}-\text{H}$ asymmetrical bending [40], respectively. The band at 1092 cm^{-1} is corresponding to $\text{C}-\text{O}$ stretching of ester. The peak around 783 cm^{-1} may be assigned to the bending of hydrogen in various locations in the aromatic rings and the peak at 990 cm^{-1} are assigned to $\text{C}-\text{O}$ [41]. The band at 1092 and 990 cm^{-1} becomes strengthened after 200°C HTC, which is probably because of the intramolecular dehydration and intermolecular [40]. The functional groups of SL and 200-hydrochar also measured by XPS (Fig. S3 and Table S1). The content of $\text{C}-\text{C}$ and $\text{C}=\text{O}$ increased after 200°C HTC pre-treatment. The peaks at 1092 and 783 cm^{-1} were weakened even disappeared after KOH activation, which is due to the dehydration during KOH activation. Sevilla and Mokaya [42] reported that KOH works not only as a dehydrating agent but also as oxidant agent during the activation process. The Raman spectra of PCs samples with different activation temperatures are shown in Fig. 3b. There are two broad bands at 1345 cm^{-1} and 1587 cm^{-1} which are correspond to the D-band and G-band, respectively. D-band is attributed to the disordered graphite and G-band is considered to be phonon mode with E_{2g} symmetry of graphite [43]. The I_D/I_G represented the defect degree of the carbon materials. The intensity ratio of 200-HTC-600-3, 200-HTC-700-3, 200-HTC-800-3 and 200-HTC-900-3 is 0.78, 0.84, 0.85 and 0.87, respectively. The slight increase of I_D/I_G value with the increasing of activation temperature, which should due to the harsh activation process by KOH [44].

3.2. Textural properties and electrochemical performance

3.2.1. Effect of HTC temperature

The effects of HTC temperature, KOH-hydrochar ratio and activation temperature on the yield and porous structure of PCs are shown in Table 2. Due to the appropriate HTC temperature, 200-HTC-800-3 reaches the largest SSA of $3069\text{ m}^2\text{ g}^{-1}$ and pore volume of $1.68\text{ cm}^3\text{ g}^{-1}$ which is much higher than that of AC-800-3 ($2239\text{ m}^2\text{ g}^{-1}$ and $1.22\text{ cm}^3\text{ g}^{-1}$). The yield of AC-800-3 is relatively low might be due to the evaporation of volatile at 800°C , which results in low yield of AC.

As shown in Fig. 4a, all the samples exhibit type I isotherm curves according to the IUPAC classification. The N_2 adsorption mainly occurs at a relative pressure less than 0.4, then a horizontal platform at high relative pressure, illustrating that PCs are mainly micropores. The SSA increased with the HTC from 160 to 200°C , while decreased when the HTC temperature above 200°C . It might be because that the increase in hydrothermal temperature leads to aromatization and high degree of aromatization. Accordingly, the chemical stability and structure order are enhanced, leading to a reduced porosity development [20]. Furthermore, the SSA of PCs is larger than AC-800-3 because the hydrochar has a small number of micropores after HTC [45]. After activated by KOH, more new pores are formatted and the existing pores were enlarged, leading to the increase of SSA. The pore size distribution is shown in Fig. 5a. Obviously, all the PCs are mainly micropores and a small amount of mesopores.

The GCD curves of PCs with different HTC temperatures at a current density of 100 mA g^{-1} in a potential range of 0 – 0.9 V are shown in Fig. 6a. All the curves exhibit symmetric triangle and linear behavior without significant IR drops, which demonstrate good capacitive performance of EDLC [35]. Similar result can also

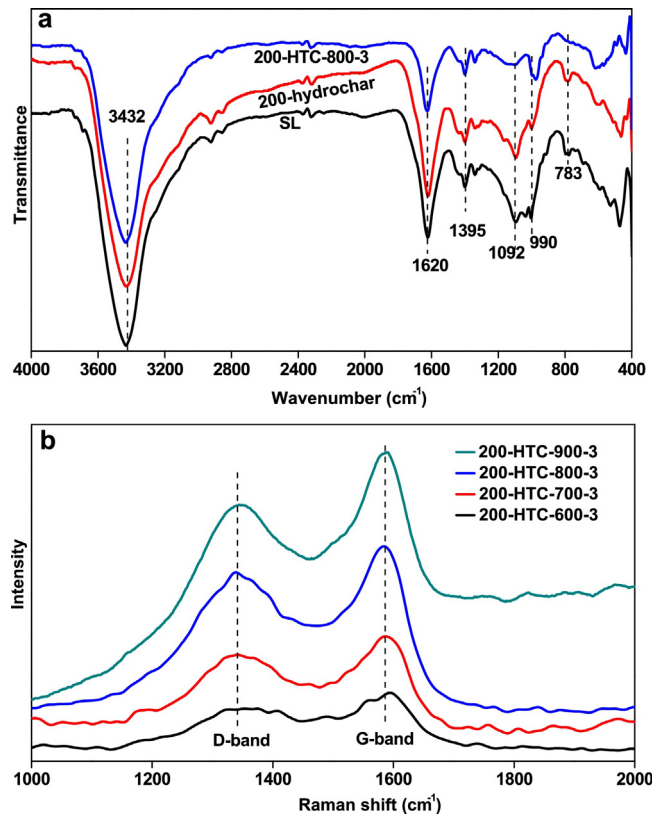


Fig. 3. FTIR spectra of SL, 200-hydrochar and 200-HTC-800-3 (a) and Raman spectra of the PCs with different activation temperatures (b).

Table 2
SSA, pore structure and yield of PCs.

Sample	$S_{\text{BET}}^{\text{a}}$ ($\text{m}^2 \text{g}^{-1}$)	V_t^{b} ($\text{cm}^3 \text{g}^{-1}$)	$S_{\text{micro}}^{\text{c}}$ ($\text{m}^2 \text{g}^{-1}$)	$S_{\text{meso}}^{\text{d}}$ ($\text{m}^2 \text{g}^{-1}$)	$V_{\text{micro}}^{\text{c}}$ ($\text{cm}^3 \text{g}^{-1}$)	$V_{\text{meso}}^{\text{d}}$ ($\text{cm}^3 \text{g}^{-1}$)	D_{ave} (nm)	Υ (%)
AC-800-3	2239	1.22	2021	218	0.97	0.25	2.19	4.1
160-HTC-800-3	2535	1.32	2354	181	1.08	0.24	2.09	12.4
180-HTC-800-3	2810	1.35	2658	152	1.17	0.18	1.92	9.7
200-HTC-800-3	3069	1.68	2747	322	1.33	0.35	2.19	8.4
220-HTC-800-3	2409	1.22	2251	158	1.04	0.18	1.86	5.3
200-HTC-800-1	1703	1.09	1513	190	0.60	0.49	2.54	29.7
200-HTC-800-2	2113	1.24	1830	283	0.83	0.41	2.35	13.9
200-HTC-800-4	3162	2.20	1456	1706	0.74	1.46	2.78	7.4
200-HTC-600-3	1805	0.83	1704	101	0.70	0.13	1.83	18.3
200-HTC-700-3	2473	1.21	2299	174	0.99	0.22	1.96	11.4
200-HTC-900-3	2466	1.46	1830	636	0.90	0.56	2.36	5.3

^a Total specific surface area calculated by BET method.

^b Total pore volume was determined at a relative pressure of $P/P_0 = 0.99$.

^c Micropores specific surface area and micropore volume calculated by t-plot method.

^d Difference of S_{BET} and S_{micro} and total pore volume and V_{micro} , respectively.

be drawn from Nyquist plot for PCs with different HTC temperatures (Fig. S4a). The curves are nearly vertical to the Z' axis at low frequency range. The charge-transfer resistance decreased with the increase in HTC temperature, which should be due to the difference in SSA and pore volume. As shown in Fig. 6a, the charge-discharge time of 200-HTC-800-3 is much longer than others, indicating that the 200-HTC-800-3 has higher C_s at the same current density, which should be partly due to the largest SSA of 200-HTC-800-3 (Fig. S1). In general, a large SSA of carbon materials leads to a large C_s [46,47]. The variation of C_s with different current densities is displayed in Fig. 6b. The C_s decreased with the increase in current density, because of the formation of electric double layer on the surface of PC requires the movement of electrolyte ions. With the increase of current density, the electro-migration resistance to the microporous increases, leading to the SSA of the PCs cannot be fully utilized [48]. The CV curves of PCs are depicted in Fig. 6c. All the curves show a similar rectangular shape without obviously redox peaks at the scan rate of 2 mV s^{-1} in a voltage ranging from 0 to 0.9 V, indicating that the electrode has good properties and the C_s of EDLC is provided by double layer capacity [49,50]. The CV curve with a larger area represent a higher C_s [51]. The 200-HTC-800-3 has the largest area of CV curve suggesting that the 200-HTC-800-3 has higher C_s at the same scanning rate in the same potential window. The result can also be derived from GCD curves in Fig. 6a.

3.2.2. Effect of KOH-hydrochar ratio

KOH-hydrochar ratio is an important factor to the pore structure and the electrochemical performance. Fig. 4b depicts the N_2 adsorption-desorption isotherms of PCs with different ratios. All the samples are mainly microporous, which are proved by the type I isotherms. There is apparent hysteresis loop in PCs when the relative pressure exceeds 0.4, which shows the presence of a certain amount of mesopores [52]. Raising the KOH-hydrochar ratio from 1:1 to 4:1 caused the increase of both the total pore volume and mesopores SSA (Table 2), indicating that the KOH-hydrochar ratio had a significant influence on the mesopores. The result can also be confirmed by the pore size distribution in Fig. 5b. The pore size of 200-HTC-800-1 and 200-HTC-800-2 is mainly concentrated in the range of 0.7 to 2.5 nm, while that of 200-HTC-800-3 and 200-HTC-800-4 is mainly between 0.7 to 5 nm, especially for 200-HTC-800-4, which has large amount of pore at 2.5 to 5 nm. Excessive KOH (the ratio of KOH-hydrochar over 3) occurs mainly the expanding of existing pores, causing relatively large pore size ($D_{\text{ave}} = 2.78 \text{ nm}$). Generally, there are three main stages of pore formation in the activation process: (1) opening of

previously inaccessible pores, (2) formation of new pores, (3) expanding of existing pores [53]. At relatively low KOH-hydrochar ratio, the stages (1) and (2) make contribution to the formation of pores. With the increase of KOH-hydrochar ratio, the stage (3) may take the domination in the reaction. The yield of PCs decreased with the increase in the mass ratio of KOH-hydrochar. There are a series of reactions during the KOH activation process as shown in below [7,54]: $2\text{KOH} \rightarrow \text{K}_2\text{O} + \text{H}_2\text{O}$, $\text{C} + \text{H}_2\text{O} \rightarrow \text{CO} + \text{H}_2$, $\text{CO} + \text{H}_2\text{O} \rightarrow \text{CO}_2 + \text{H}_2$, $6\text{KOH} + 2\text{C} \rightarrow 2\text{K} + 3\text{H}_2 + 2\text{K}_2\text{CO}_3$. When the activation temperature over 700°C will also occur the following reactions: $\text{K}_2\text{CO}_3 \rightarrow \text{CO}_2 + \text{K}_2\text{O}$, $\text{CO}_2 + \text{C} \rightarrow 2\text{CO}$, $\text{K}_2\text{CO}_3 + 2\text{C} \rightarrow 2\text{K} + 3\text{CO}$. With the KOH amount increases, an increasing number of carbon atoms in SL reacted with KOH, which caused the decrease of PC yield and the increase of SSA and pore volume.

Fig. 7a displays the GCD curves of the PCs with different KOH-hydrochar ratios at a current density of 100 mA g^{-1} . All the samples show high linear and approximately symmetric, indicating the electrodes prepared from the PCs have typical capacitive behavior and good reversibility. The C_s firstly increased from 223 to 295 F g^{-1} when raising the KOH-hydrochar ratio from 1 to 3 and then decreased to 271 F g^{-1} when the ratio is up to 4. Although 200-HTC-800-4 has the highest SSA but it has a large number of pore at 2.5 to 5.0 nm, which has low contribution to the C_s . The SSA is an important factor, but some other properties such as pore size distribution, pore structure, electrical conductivity and surface functionality also affect the electrochemical properties of EDLC [8]. The pore size close to the ion size lead to the maximum C_s and both larger and smaller pores result in a drop in C_s [55]. Zhao et al. [10] reported that the activated carbons with pore size at 1–2 nm has higher C_s than that larger than 2 nm. Chmiola et al. [56] reported that increasing the volume of pore smaller than 2 nm is conducive to the increase of C_s , while increasing the volume of pores larger than 2 nm at the expense of smaller pores has a detrimental effect on C_s . The relationship between C_s and current density is shown in Fig. 7b. The C_s decreased with the increase in current density. The charge-discharge time at high current density is relatively short and the ions in the electrolyte have difficulty entering into the pores in a limited time [6]. The 200-HTC-800-4 decreased fast at high current densities, which might be due to the low micropores SSA of 200-HTC-800-4. Chmiola et al. [57] reported that the micropores contribute more to EDLC C_s than mesopores, because of the dissociation of solvation shell. The electrochemical property of PCs was further tested by CV. As can be seen from Fig. 7c, all the CV curves present approximate rectangular shape without apparent redox peaks reflecting the C_s is mainly provided by the double layer. Furthermore, the CV area of 200-HTC-800-3 was

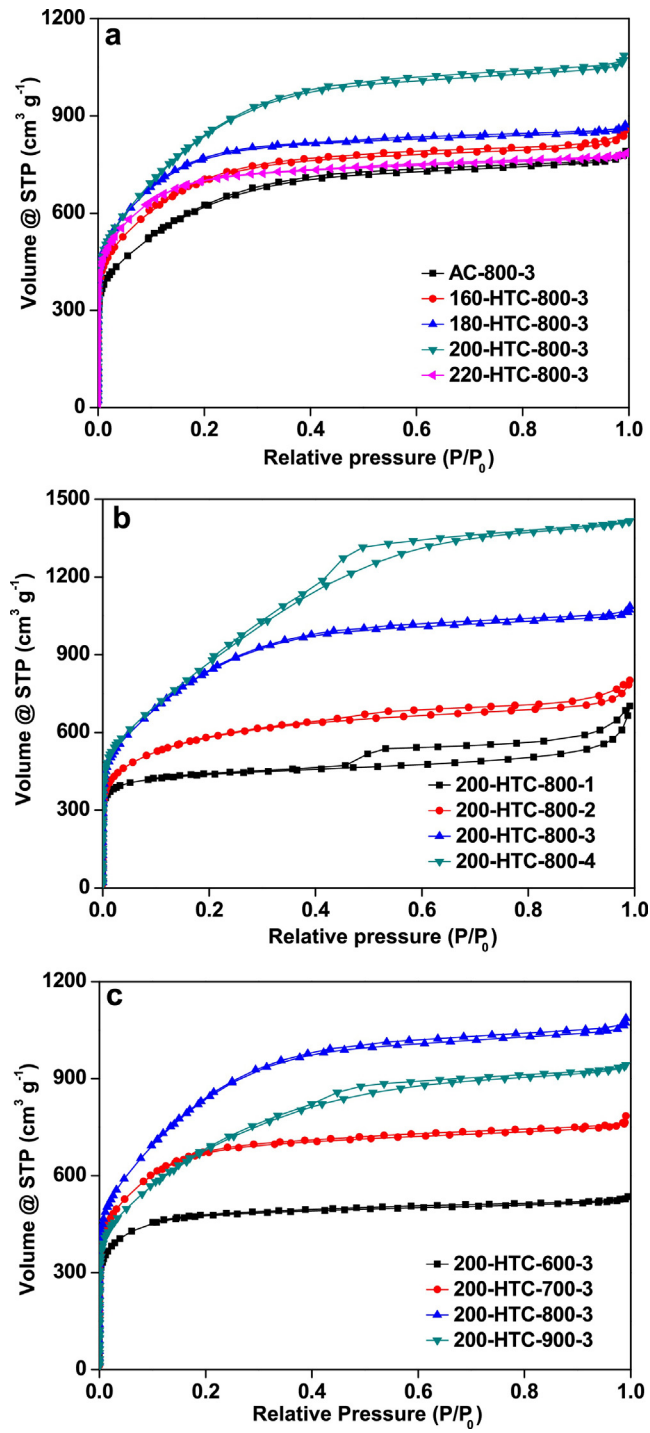


Fig. 4. N_2 adsorption-desorption isotherm curves of PCs.

larger than others, indicating the highest C_s of 200-HTC-800-3, which can also be confirmed by GCD curve in Fig. 7a. The charge-transfer resistance decreased with the increase in KOH-hydrochar ratio (Fig. S4b) due to the enhanced SSA and total pore volume. The curve of 200-HTC-800-3 electrode at the low frequency range is nearly straight line, indicating a good capacitance behavior.

3.2.3. Effect of activation temperature

In this part, the PCs were prepared under the activation temperature from 600 to 900 °C with the KOH-hydrochar mass ratio of 3. As exhibited in Table 2, the SSA and micropores volume

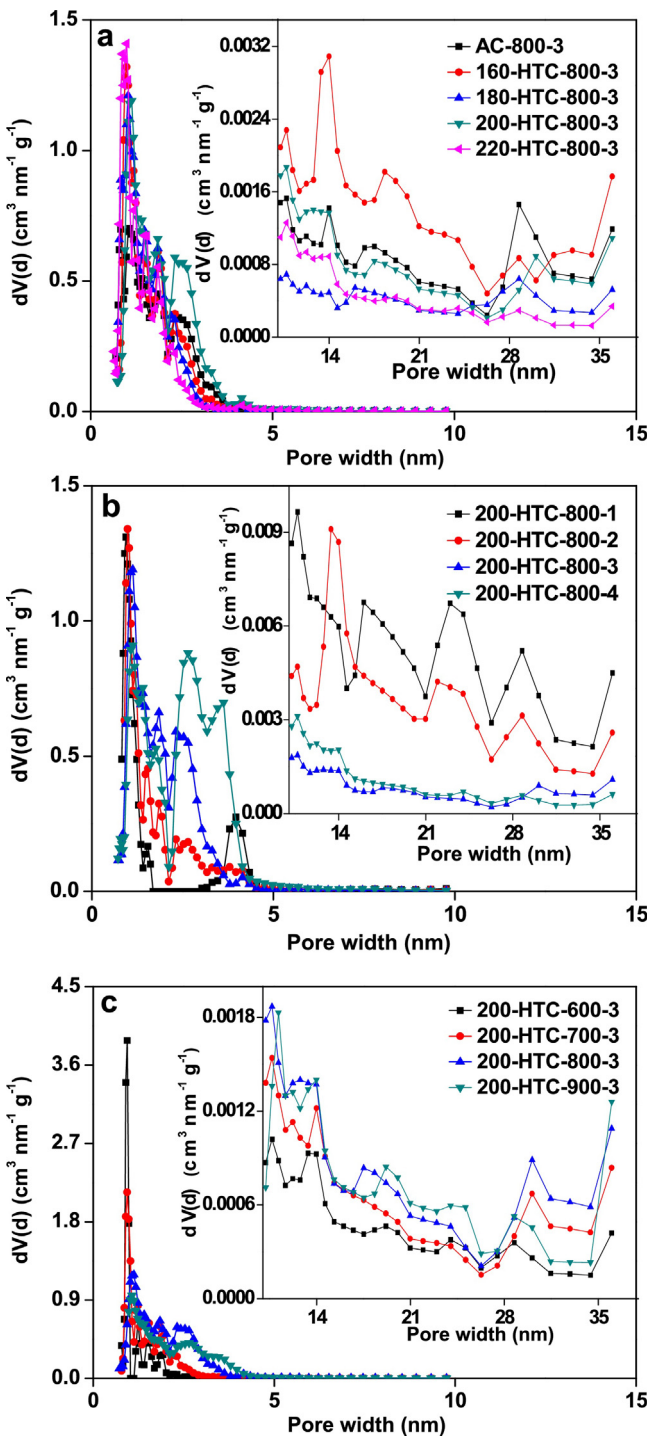


Fig. 5. Pore size distribution of PCs.

increased with the increase of the activation temperature from 600 to 800 °C, and then decreased when the activation temperature was further increased above 800 °C. The reaction between KOH and carbon requires high energy, so the reaction may be not complete at low temperature (600 °C) and result in a small pore size and low SSA. When the temperature reached 700 and 800 °C, the reaction becomes violent and more pores are formed, which caused the increase of SSA. However, excessively high temperature (900 °C) causes the collapse and destruction of pores and micropores are enlarged into mesopores even macropores due to the severe

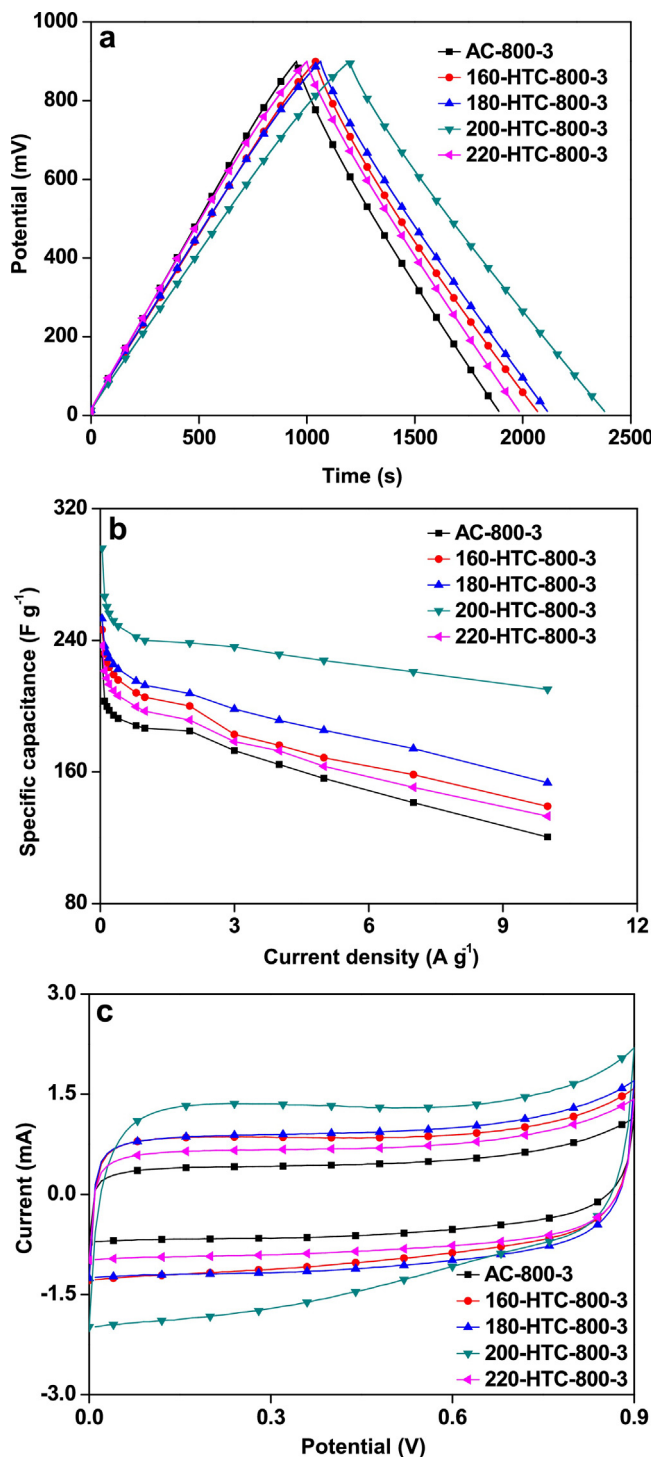


Fig. 6. Impact of HTC temperature on electrochemical performance. GCD curves of PCs at 100 mA g^{-1} (a), the C_s s of PCs at different current densities (b) and CV curves of PCs at 2 mV s^{-1} (c).

thermal treatment and extensive reaction and thus decreases the SSA and increases the mesopore volume [53]. It can also be seen from Table 2, the yield of PCs decreased progressively when raising the activation temperature from 600 to 900 °C, which should be due to the enhancement of volatile products release and “burn-off” of carbon via the C-KOH reaction [58]. As shown in Fig. 4c, the N_2 adsorption volume increased sharply with the increase of the relative pressure below 0.2, demonstrating the PCs are mainly

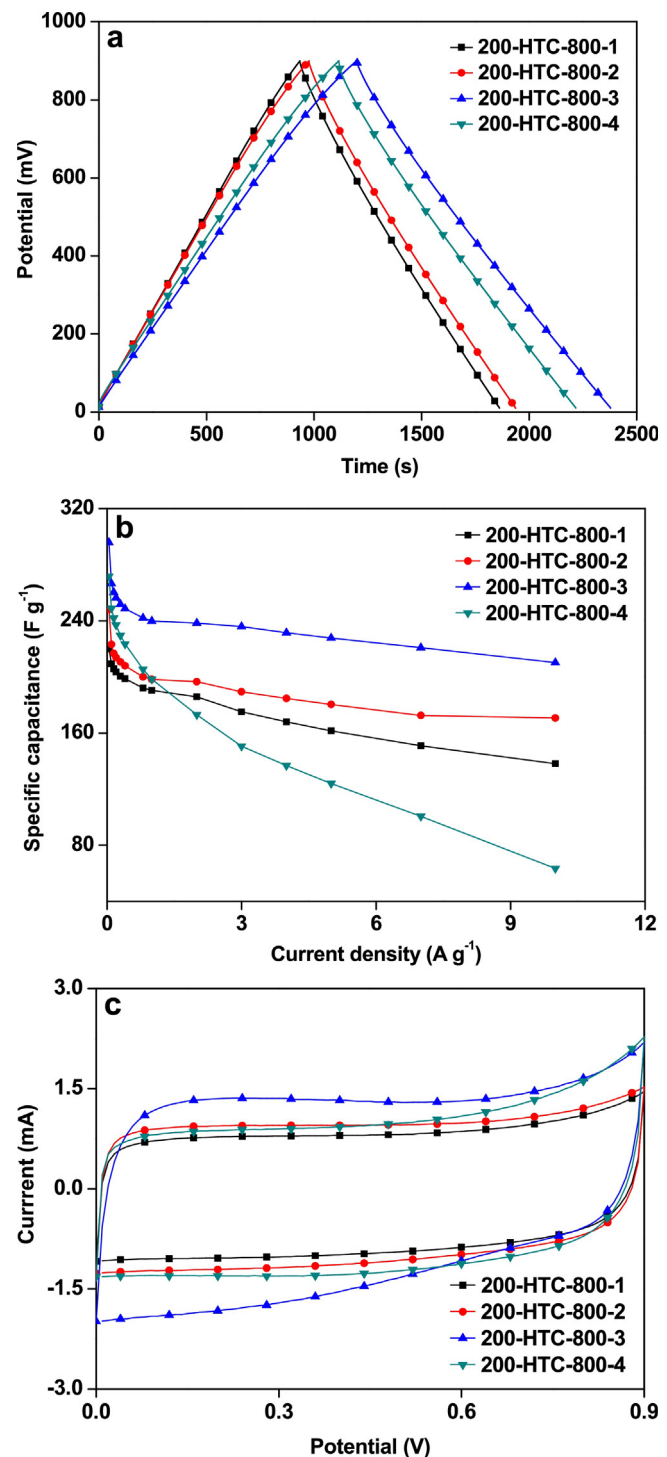


Fig. 7. Impact of KOH-hydrochar ratio on electrochemical performance. GCD curves of PCs at 100 mA g^{-1} (a), the C_s s of PCs at different current densities (b) and CV curves of PCs at 2 mV s^{-1} (c).

microporous materials. Fig. 5c shows the pore size distributions for four PCs, mostly ranging from 0.7 to 2.5 nm.

As shown in Fig. 8a, all the GCD curves present linearity and regular triangular ships, indicating good EDLC behavior. The charge-discharge time of 200-HTC-800-3 is longer than others. This prove that 200-HTC-800-3 can be charged with more electrolyte ions, indicating the higher C_s . According to Eq. (2), the C_s was calculated from the slope of the discharge time under

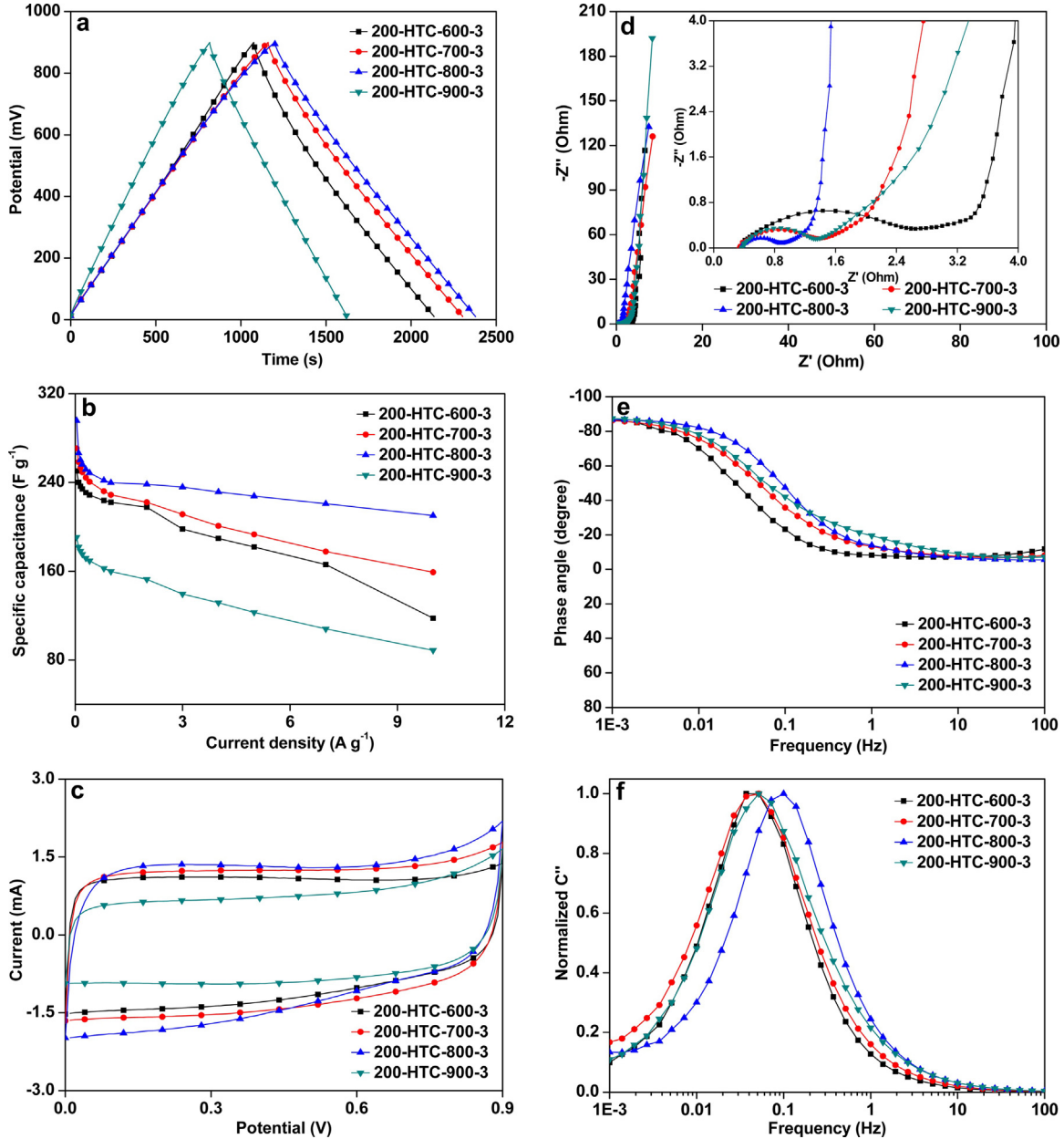


Fig. 8. Impact of activation temperature on electrochemical performance. GCD curves of PCs at 100 mA g⁻¹ (a), the C_s of PCs at different current densities (b), CV curves of PCs at 2 mV s⁻¹ (c), Nyquist plot for PCs (d), impedance phase angle versus frequency (e) and normalized imaginary part capacitance (f).

different current densities, which is shown in Fig. 8b. The C_s of 200-HTC-600-3, 200-HTC-700-3, 200-HTC-800-3 and 200-HTC-900-3 is 250, 270, 295 and 190 F g⁻¹, respectively, at the current density of 40 mA g⁻¹. And the C_s of the four PCs retained 117, 159, 210 and 88 F g⁻¹ at 10 A g⁻¹, demonstrating 800 °C is the most suitable activation temperature for PC preparation. The pore volume and SSA are relatively small at low activation temperature and the charge transfer resistance of electrolyte ions are relatively large, which leads to the fast drop of C_s . Furthermore, the CV curve of 200-HTC-800-3 approaches to a rectangular shape and has the largest area (Fig. 8c), demonstrating the good electrochemical performance of 200-HTC-800-3.

The Nyquist plots of PCs with different activation temperatures in the frequency range of 10^{-3} to 10^6 Hz under open circuit potential is exhibited in Fig. 8d and the equivalent circuit model based on the 200-HTC-800-3 EIS data is shown in Fig. S5. The

equivalent circuit model of EDLC shows that the circuit of the EDLC capacitor consisted of L, R_s , W, R_{ct} , C and Q. As can be seen from Fig. 8d, all the plots display a semicircle at high frequency and vertical slope at the low-frequency region. The value of the four curves intersection with the real axis are approximately the same, indicating that the ionic resistance of electrolyte and the contact resistance are similar. Because all of the EDLC use the 6 M KOH as electrolyte and the method of assembly is the same. The semicircle represents the charge-transfer resistance, which is related to electric conductivity and the porous structure [59]. The charge-transfer resistance of 200-HTC-800-3 is relatively lower than other samples. At medium frequency, a slope of about 45° is Warburg impedance and the projected length of Warburg line on the real axis represent the diffusion of ions at the electrode-electrolyte interface [29,60]. As shown in Fig. 8d, the 200-HTC-800-3 has relatively short Warburg line, indicating fine ion diffusion in micro-

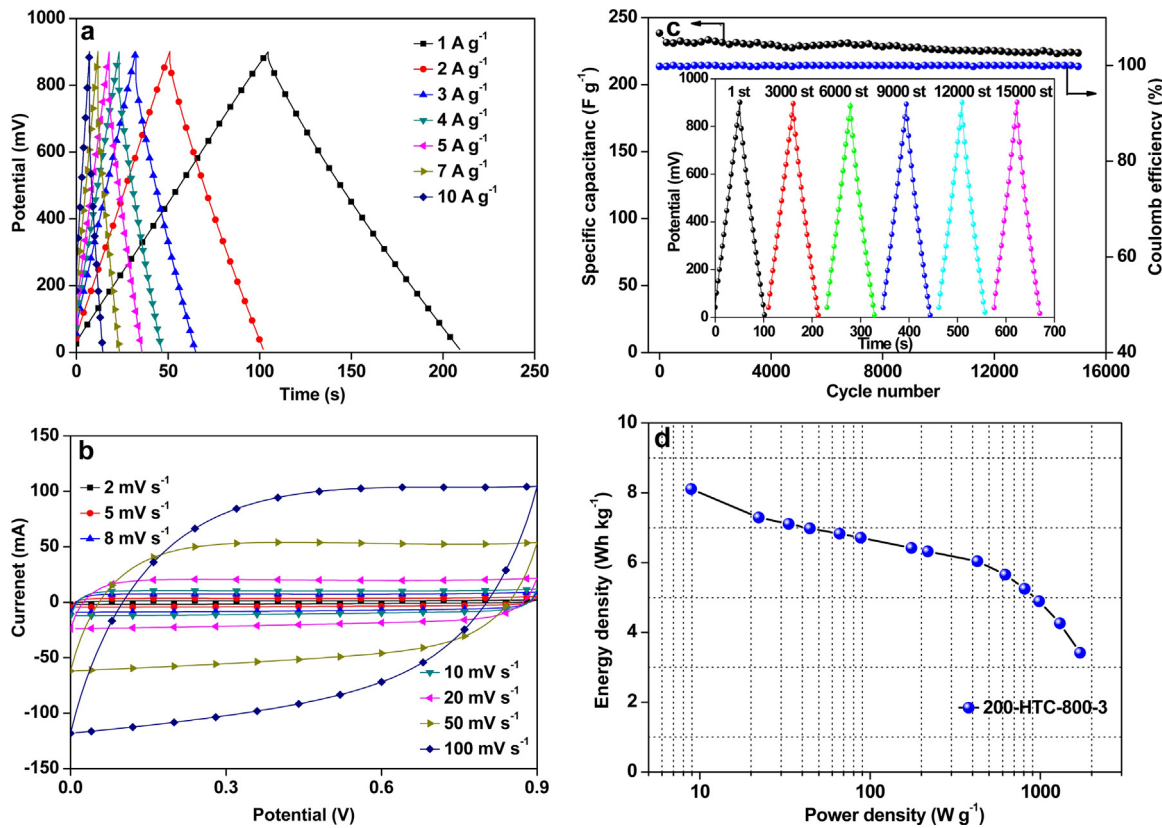


Fig. 9. GCD curves of 200-HTC-800-3 at different current densities (a), CV curves of 200-HTC-800-3 at different sweep rates (b) and cycle life of 200-HTC-800-3 at current density of 2 A g^{-1} (c), Ragone plot of 200-HTC-800-3 device at different current density (d).

mesoporous structure of the 200-HTC-800-3. The lines are nearly vertical to the Z' axis at low-frequency region, indicating the PCs electrodes have good electrochemical capacitance behavior, which also can be proved by Fig. 8e. The phase angle of all the PCs are close to -90° at low frequency. Fig. 8f illustrates the normalized imaginary capacitance with frequency. The relaxation time constant (τ_0) can be calculated from the frequency (ω) at the maximum value. The ω is 0.10 Hz for the 200-HTC-800-3 (Eqs. (5)–(7)) corresponding to the $\tau_0 = 10.0 \text{ s}$, which indicates the good electrical conductivity and excellent rate capability of 200-HTC-800-3.

Fig. 9a displays the GCD curves of 200-HTC-800-3 at different current densities. It can be seen that all the curves are approximately linear and symmetrical when the current density was increased from 1 to 10 A g^{-1} , showing the electrode prepared by the 200-HTC-800-3 has excellent capacitive behavior. Fig. 9b shows the CV curves of 200-HTC-800-3 with scan rates from 2 to 100 mV s^{-1} . The CV curves become deviation from the rectangular shape when the sweep rates to 100 mV s^{-1} due to the limitation in

charge transfer process at higher scan rate [61]. Fig. 9c shows the cycling performance and coulomb efficiency of 200-HTC-800-3 under a current density of 2 A g^{-1} . The sample shows excellent cycling performance and almost no decay after 15000 cycles and about 93.8% of initial C_s is retained. The coulomb efficiency was calculated as follow equation.

$$\eta = \frac{T_d}{T_c} \times 100\% \quad (8)$$

T_d and T_c are the discharge time and charge time, respectively. The value of coulomb efficiency is 99.8% after 15000 cyclic charge-discharge processes, which further indicating the 200-HTC-800-3 has excellent electrochemical stability and coulomb efficiency. The energy density and power density of 200-HTC-800-3 were calculated by Eqs. (3) and (4) (Fig. 9d). It can be seen that the 200-HTC-800-3 shows an energy density of 8.11 Wh kg^{-1} , which is owing to its high C_s at current density of 40 mA g^{-1} .

In comparison with the recently reported PC electrode materials (Table 3), the PCs prepared from lignite by HTC pre-

Table 3
PCs for EDLC electrodes.

Raw materials	S_{BET} ($\text{m}^2 \text{ g}^{-1}$)	Current density (mA g^{-1})	C_s (F g^{-1})	Cell configuration No. electrodes	Electrolyte	Ref.
Coal tar pitch	1985	50	277	2	6 M KOH	[62]
Enteromorpha	1651	50	206	2	6 M KOH	[6]
Lignite	1024	500	207.5	3	6 M KOH	[63]
Coal tar	1865	50	274	2	6 M KOH	[64]
Ultra-Pure lignite	1696	20	189	2	6 M KOH	[65]
Coal tar	3235	50	296.2	2	6 M KOH	[66]
Lignite	3069	40	295	2	6 M KOH	This work

treatment and KOH activation are highly promising as electrode for EDLC and present excellent electrochemical performance at the aqueous electrolytes, which is owed to the relatively high SSA, suitable pore size distribution and low impedance of PCs.

4. Conclusion

The lignite pretreated by HTC is an excellent precursor for the preparation of PCs via KOH activation. The obtained PCs exhibit higher SSA and pore volume compared with the common preparation process in the absence of hydrothermal treatment. The porosity development and pore size distribution were extremely affected by the HTC temperature. The C_s not only affected by SSA but also affected by pore size distribution. The highest C_s of 200-HTC-800-3 is 295 F g^{-1} at a current density of 40 mA g^{-1} . 200-HTC-800-3 can achieve a relatively high rate capability, which is about 71.0% retention at a current density of 10 A g^{-1} . It also shows excellent cycling stability with 93.8% C_s retention after 15000 charge-discharge cycles. This work demonstrates that the lignite-derived PCs have promising potential for energy storage devices.

Acknowledgements

This work was subsidized by the Fundamental Research Funds for the Central Universities (China University of Mining & Technology, Grant 2015XKMS043), National Natural Science Foundation of China (Grant 21676292), Natural Science Foundation of Jiangsu Province (BK20161180), and the Priority Academic Program Development of Jiangsu Higher Education Institutions.

Appendix A. Supplementary data

Supplementary data associated with this article can be found, in the online version, at <http://dx.doi.org/10.1016/j.electacta.2017.08.176>.

References

- [1] H.N. Wang, J. Varghese, L. Pilon, Simulation of electric double layer capacitors with mesoporous electrodes: Effects of morphology and electrolyte permittivity, *Electrochim. Acta* 56 (2011) 6189–6197.
- [2] X.L. Gao, W. Xing, J. Zhou, G.Q. Wang, S.P. Zhuo, Z. Liu, Q.Z. Xue, Z.F. Yan, Superior capacitive performance of active carbons derived from *Enteromorpha prolifera*, *Electrochim. Acta* 133 (2014) 459–466.
- [3] G. Pognon, T. Brousse, D. Bélanger, Effect of molecular grafting on the pore size distribution and the double layer capacitance of activated carbon for electrochemical double layer capacitors, *Carbon* 49 (2011) 1340–1348.
- [4] X.Y. Zhao, S.S. Huang, J.P. Cao, S.C. Xi, X.Y. Wei, J. Kamamoto, T. Takarada, KOH activation of a HyperCoal to develop activated carbons for electric double-layer capacitors, *J. Anal. Appl. Pyrol.* 105 (2014) 116–121.
- [5] A.K. Shukla, A. Banerjee, M.K. Ravikumar, A. Jalajakshi, Electrochemical capacitors: Technical challenges and prognosis for future markets, *Electrochim. Acta* 84 (2012) 165–173.
- [6] M.B. Wu, P. Li, Y. Li, J. Liu, Y. Wang, Enteromorpha based porous carbons activated by zinc chloride for supercapacitors with high capacity retention, *RSC Adv.* 5 (2015) 16575–16581.
- [7] Y.H. Cao, K.L. Wang, X.M. Wang, Z.R. Gu, Q.H. Fan, W. Gibbons, J.D. Hoefelmeyer, P.R. Kharel, M. Shrestha, Hierarchical porous activated carbon for supercapacitor derived from corn stalk core by potassium hydroxide activation, *Electrochim. Acta* 212 (2016) 839–847.
- [8] L.L. Zhang, X.S. Zhao, Carbon-based materials as supercapacitor electrodes, *Chem. Soc. Rev.* 38 (2009) 2520–2531.
- [9] H. Jin, X.M. Wang, Z.R. Gu, J.D. Hoefelmeyer, K. Muthukumarappan, J. Julson, Graphitized activated carbon based on big bluestem as an electrode for supercapacitors, *RSC Adv.* 4 (2014) 14136–14142.
- [10] X.Y. Zhao, S.S. Huang, J.P. Cao, X.Y. Wei, K. Magarisawa, T. Takarada, HyperCoal-derived porous carbons with alkaline hydroxides and carbonate activation for electric double-layer capacitors, *Fuel Process. Technol.* 125 (2014) 251–257.
- [11] K. Babel, K. Jurewicz, Electrical capacitance of fibrous carbon composites in supercapacitors, *Fuel Process. Technol.* 77 (2002) 181–189.
- [12] Z.Q. Hao, J.P. Cao, Y. Wu, X.Y. Zhao, L. Zhou, X. Fan, Y.P. Zhao, X.Y. Wei, Preparation of porous carbons from waste sugar residue for high performance electric double-layer capacitor, *Fuel Process. Technol.* 162 (2017) 45–54.
- [13] A. Izadi-Najafabadi, T. Yamada, D.N. Futaba, M. Yudasaka, H. Takagi, H. Hatori, S. Iijima, A. Hata, High-power supercapacitor electrodes from single-walled carbon nanohorn/nanotube composite, *ACS Nano* 5 (2011) 811–819.
- [14] E. Frackowiak, K. Jurewicz, K. Szostak, S. Delpeux, F. Be'guin, Nanotubular materials as electrodes for supercapacitors, *Fuel Process. Technol.* 77 (2002) 213–219.
- [15] T. Kim, G. Jung, S. Yoo, K.S. Suh, R.S. Ruoff, Activated graphene-based carbons as supercapacitor electrodes with macro-and mesopores, *ACS Nano* 7 (2013) 6899–6905.
- [16] Q. Cheng, J. Tang, J. Ma, H. Zhang, N. Shinya, L.C. Qin, Graphene and nanostructured MnO₂ composite electrodes for supercapacitors, *Carbon* 49 (2011) 2917–2925.
- [17] T.T. Chen, W.L. Song, L.Z. Fan, Engineering graphene aerogels with porous carbon of large surface area for flexible all-solid-state supercapacitors, *Electrochim. Acta* 165 (2015) 92–97.
- [18] C. Tran, V. Kalra, Fabrication of porous carbon nanofibers with adjustable pore sizes as electrodes for supercapacitors, *J. Power Sources* 235 (2013) 289–296.
- [19] C. Falco, F. Perez Caballero, F. Babonneau, C. Gervais, G. Laurent, M.M. Titirici, N. Baccile, Hydrothermal carbon from biomass: Structural differences between hydrothermal and pyrolyzed carbons via ¹³C solid state NMR, *Langmuir* 27 (2011) 14460–14471.
- [20] C. Falco, J.P. Marco-Lozar, D. Salinas-Torres, E. Morallón, D. Cazorla-Amorós, M. M. Titirici, D. Lozano-Castelló, Tailoring the porosity of chemically activated hydrothermal carbons: Influence of the precursor and hydrothermal carbonization temperature, *Carbon* 62 (2013) 346–355.
- [21] A. Jain, C. Xu, S. Jayaraman, R. Balasubramanian, J.Y. Lee, M.P. Srinivasan, Mesoporous activated carbons with enhanced porosity by optimal hydrothermal pre-treatment of biomass for supercapacitor applications, *Microporous Mesoporous Mat.* 218 (2015) 55–61.
- [22] Z.G. Liu, F.S. Zhang, J.Z. Wu, Characterization and application of chars produced from pinewood pyrolysis and hydrothermal treatment, *Fuel* 89 (2010) 510–514.
- [23] B.R. Selvi, D. Jagadeesan, B.S. Suma, G. Nagashankar, M. Arif, K. Balasubramanyam, M. Eswaramoorthy, T.K. Kundu, Intrinsically fluorescent carbon nanospheres as a nuclear targeting vector: Delivery of membrane-impermeable molecule to modulate gene expression in vivo, *Nano Lett.* 8 (2008) 3182–3188.
- [24] X. Wang, C.G. Hu, Y.F. Xiong, H. Liu, G.J. Du, X.S. He, Carbon-nanosphere-supported Pt nanoparticles for methanol and ethanol electro-oxidation in alkaline media, *J. Power Sources* 196 (2011) 1904–1908.
- [25] M.M. Titirici, M. Antonietti, A. Thomas, A generalized synthesis of metal oxide hollow spheres using a hydrothermal approach, *Chem. Mater.* 18 (2006) 3808–3812.
- [26] M. Sevilla, J.A. Maciá-Agulló, A.B. Fuertes, Hydrothermal carbonization of biomass as a route for the sequestration of CO₂: Chemical and structural properties of the carbonized products, *Biomass Bioenergy* 35 (2011) 3152–3159.
- [27] M. Sevilla, A.B. Fuertes, R. Mokaya, High density hydrogen storage in superactivated carbons from hydrothermally carbonized renewable organic materials, *Energ. Environ. Sci.* 4 (2011) 1400–1410.
- [28] A. Jain, S. Jayaraman, R. Balasubramanian, M.P. Srinivasan, Hydrothermal pre-treatment for mesoporous carbon synthesis: Enhancement of chemical activation, *J. Mater. Chem. A2* (2014) 520–528.
- [29] Y. Fan, X. Yang, B. Zhu, P.F. Liu, H.T. Lu, Micro-mesoporous carbon spheres derived from carrageenan as electrode material for supercapacitors, *J. Power Sources* 268 (2014) 584–590.
- [30] M. Entríá, M.F.R. Pereira, J.I. Martins, J.L. Figueiredo, Hydrothermal functionalization of ordered mesoporous carbons: The effect of boron on supercapacitor performance, *Carbon* 95 (2015) 72–83.
- [31] Z.Q. Hao, J.P. Cao, Y. Wu, X.Y. Zhao, Q.Q. Zhuang, X.Y. Wang, X.Y. Wei, Preparation of porous carbon sphere from waste sugar solution for electric double-layer capacitor, *J. Power Sources* 361 (2017) 249–258.
- [32] G.K. Parshetti, A. Quek, R. Betha, R. Balasubramanian, TGA-FTIR investigation of co-combustion characteristics of blends of hydrothermally carbonized oil palm biomass (EFB) and coal, *Fuel Process. Technol.* 118 (2014) 228–234.
- [33] H. Katalambula, R. Gupta, Low-grade coals: A review of some prospective upgrading technologies, *Energ. Fuels* 23 (2009) 3392–3405.
- [34] P.L. Taberna, P. Simon, J.F. Fauvarque, Electrochemical characteristics and impedance spectroscopy studies of carbon-carbon supercapacitors, *J. Electrochim. Soc.* 150 (2003) A292–A300.
- [35] W.J. Lu, M.X. Liu, L. Miao, D.Z. Zhu, X. Wang, H. Duan, Z.W. Wang, L.C. Li, Z.J. Xu, L.H. Gan, L.W. Chen, Nitrogen-containing ultramicroporous carbon nanospheres for high performance supercapacitor electrodes, *Electrochim. Acta* 205 (2016) 132–141.
- [36] Y.H. Yang, J.H. Cui, M.T. Zheng, C.F. Hu, S.Z. Tan, Y. Xiao, Q. Yang, Y.L. Liu, One-step synthesis of amino-functionalized fluorescent carbon nanoparticles by hydrothermal carbonization of chitosan, *Chem. Commun.* 48 (2012) 380–382.
- [37] X. Du, L. Wang, W. Zhao, Y. Yang, T. Qi, C.M. Li, Preparation of hierarchical porous carbon from waste printed circuit boards for high performance electric double-layer capacitors, *J. Power Sources* 323 (2016) 166–173.
- [38] M.M. Xu, Q.B. Huang, R.C. Sun, X.H. Wang, Simultaneously obtaining fluorescent carbon dots and porous active carbon for supercapacitors from biomass, *RSC Adv.* 6 (2016) 88674–88682.
- [39] M. Genovese, J.H. Jiang, K. Lian, N. Holm, High capacitive performance of exfoliated biochar nanosheets from biomass waste corn cob, *J. Mater. Chem. A* 3 (2015) 2903–2913.

- [40] R.J. Mo, Y. Zhao, M. Wu, H.M. Xiao, S. Kuga, Y. Huang, J.P. Li, S.Y. Fu, Activated carbon from nitrogen rich watermelon rind for high-performance supercapacitors, *RSC Adv.* 6 (2016) 59333–59342.
- [41] B.Y. Jibril, R.S. Al-Maamari, G. Hegde, N. Al-Mandhary, O. Houache, Effects of feedstock pre-drying on carbonization of KOH-mixed bituminous coal in preparation of activated carbon, *J. Anal. Appl. Pyrol.* 80 (2007) 277–282.
- [42] M. Sevilla, R. Mokaya, Energy storage applications of activated carbons: Supercapacitors and hydrogen storage, *Energ. Environ. Sci.* 7 (2014) 1250–1280.
- [43] A. Sadezky, H. Muckenhuber, H. Grothe, R. Niessner, U. Pöschl, Raman microspectroscopy of soot and related carbonaceous materials: Spectral analysis and structural information, *Carbon* 43 (2005) 1731–1742.
- [44] J. Zhou, Z.S. Zhang, W. Xing, J. Yu, G.X. Han, W.J. Si, S.P. Zhuo, Nitrogen-doped hierarchical porous carbon materials prepared from meta-aminophenol formaldehyde resin for supercapacitor with high rate performance, *Electrochim. Acta* 153 (2015) 68–75.
- [45] M.M. Titirici, M. Antonietti, Chemistry and materials options of sustainable carbon materials made by hydrothermal carbonization, *Chem. Soc. Rev.* 39 (2010) 103–116.
- [46] O. Barbieri, M. Hahn, A. Herzog, R. Kötz, Capacitance limits of high surface area activated carbons for double layer capacitors, *Carbon* 43 (2005) 1303–1310.
- [47] A. Elmouahidi, E. Bailón-García, A.F. Pérez-Cadenas, F.J. Maldonado-Hódar, F. Carrasco-Marín, Activated carbons from KOH and H₃PO₄-activation of olive residues and its application as supercapacitor electrodes, *Electrochim. Acta* 229 (2017) 219–228.
- [48] J.J. Yoo, K. Balakrishnan, J. Huang, V. Meunier, B.G. Sumpter, A. Srivastava, M. Conway, A.L. Reddy, J. Yu, R. Vajtai, P.M. Ajayan, Ultrathin planar graphene supercapacitors, *Nano Lett.* 11 (2011) 1423–1427.
- [49] X.J. He, N. Zhang, X.L. Shao, M.B. Wu, M.X. Yu, J.S. Qiu, A layered-template-nanospace-confinement strategy for production of corrugated graphene nanosheets from petroleum pitch for supercapacitors, *Chem. Eng. J.* 297 (2016) 121–127.
- [50] Y. Gao, W.L. Zhang, Q.Y. Yue, B.Y. Gao, Y.Y. Sun, J.J. Kong, P. Zhao, Simple synthesis of hierarchical porous carbon from Enteromorpha prolifera by a self-template method for supercapacitor electrodes, *J. Power Sources* 270 (2014) 403–410.
- [51] M.X. Liu, L.H. Gan, W. Xiong, F.Q. Zhao, X.Z. Fan, D.Z. Zhu, Z.J. Xu, Z.X. Hao, L.W. Chen, Nickel-doped activated mesoporous carbon microspheres with partially graphitic structure for supercapacitors, *Energ. Fuels* 27 (2013) 1168–1173.
- [52] C. Peng, X.B. Yan, R.T. Wang, J.W. Lang, Y.J. Ou, Q.J. Xue, Promising activated carbons derived from waste tea-leaves and their application in high performance supercapacitors electrodes, *Electrochim. Acta* 87 (2013) 401–408.
- [53] J. Wang, M.M. Chen, C.Y. Wang, J.Z. Wang, J.M. Zheng, Preparation of mesoporous carbons from amphiphilic carbonaceous material for high-performance electric double-layer capacitors, *J. Power Sources* 196 (2011) 550–558.
- [54] M.A. Lillo-Rodenas, D. Cazorla-Amorós, A. Linares-Solano, Understanding chemical reactions between carbons and NaOH and KOH an insight into the chemical activation mechanism, *Carbon* 41 (2003) 267–275.
- [55] C. Largeot, C. Portet, J. Chmiola, P.L. Taberna, Y. Gogotsi, P. Simon, Relation between the ion size and pore size for an electric double-layer capacitor, *J. Am. Chem. Soc.* 130 (2008) 2730–2731.
- [56] J. Chmiola, G. Yushin, R. Dash, Y. Gogotsi, Effect of pore size and surface area of carbide derived carbons on specific capacitance, *J. Power Sources* 158 (2006) 765–772.
- [57] J. Chmiola, G. Yushin, Y. Gogotsi, C. Portet, P. Simon, P.L. Taberna, Anomalous increase in carbon capacitance at pore sizes less than 1 nanometer, *Science* 313 (2006) 1760–1763.
- [58] A.C. Lua, T. Yang, Effect of activation temperature on the textural and chemical properties of potassium hydroxide activated carbon prepared from pistachio-nut shell, *J. Colloid Interface Sci.* 274 (2004) 594–601.
- [59] S. Zhao, C.Y. Wang, M.M. Chen, J. Wang, Z.Q. Shi, Potato starch-based activated carbon spheres as electrode material for electrochemical capacitor, *J. Phys. Chem. Solids* 70 (2009) 1256–1260.
- [60] H.M. Sun, W.H. He, C.H. Zong, L.H. Lu, Template-free synthesis of renewable macroporous carbon via yeast cells for high-performance supercapacitor electrode materials, *ACS Appl. Mater. Inter.* 5 (2013) 2261–2268.
- [61] X.J. He, P.H. Ling, M.X. Yu, X.T. Wang, X.Y. Zhang, M.D. Zheng, Rice husk-derived porous carbons with high capacitance by ZnCl₂ activation for supercapacitors, *Electrochim. Acta* 105 (2013) 635–641.
- [62] X.J. He, X.J. Li, H. Ma, J.F. Han, H. Zhang, C. Yu, N. Xiao, J.S. Qiu, ZnO template strategy for the synthesis of 3D interconnected graphene nanocapsules from coal tar pitch as supercapacitor electrode materials, *J. Power Sources* 340 (2017) 183–191.
- [63] L.J. Li, X.Y. Wang, S.J. Wang, Z.Z. Cao, Z.J. Wu, H. Wang, Y.F. Gao, J.R. Liu, Activated carbon prepared from lignite as supercapacitor electrode materials, *Electroanal.* 28 (2016) 243–248.
- [64] X.Y. Xie, X.J. He, X.L. Shao, S.A. Dong, N. Xiao, J.S. Qiu, Synthesis of layered microporous carbons from coal tar by directing, space-confinement and self-sacrificed template strategy for supercapacitors, *Electrochim. Acta* 246 (2017) 634–642.
- [65] M.Y. Zhang, X. Zhao, Q.C. Zhuang, Preparation and electrochemical properties of multiscale porous active carbon for supercapacitor electrodes made from ultra-pure lignite by microwave irradiation, *Int. J. Electrochem. Sci.* 11 (2016) 2153–2165.
- [66] X.J. He, H. Ma, J.X. Wang, Y.Y. Xie, N. Xiao, J.S. Qiu, Porous carbon nanosheets from coal tar for high-performance supercapacitors, *J. Power Sources* 357 (2017) 41–46.